Rapid Communications

Scanning gate microscopy in a viscous electron fluid

B. A. Braem,[1,*] F. M. D. Pellegrino,[2,3] A. Principi,[4] M. Röösli,[1] C. Gold,[1] S. Hennel,[1] J. V. Koski,[1] M. Berl,[1] W. Dietsche,[1] W. Wegscheider,[1] M. Polini,[5] T. Ihn,[1] and K. Ensslin[1]

[1]*ETH Zürich, Solid State Physics Laboratory, Otto-Stern-Weg 1, 8093 Zürich, Switzerland*
[2]*Dipartimento di Fisica e Astronomia, Università di Catania, Via S. Sofia, 64, I-95123 Catania, Italy*
[3]*INFN, Sez. Catania, I-95123 Catania, Italy*
[4]*School of Physics and Astronomy, University of Manchester, Manchester M13 9PL, United Kingdom*
[5]*Istituto Italiano di Tecnologia, Graphene Labs, Via Morego 30, I-16163 Genova, Italy*

(Received 9 July 2018; revised manuscript received 4 December 2018; published 21 December 2018)

We measure transport through a Ga[Al]As heterostructure at temperatures between 32 mK and 30 K. Increasing the temperature enhances the electron-electron scattering rate and viscous effects in the two-dimensional electron gas arise. To probe this regime we measure so-called vicinity voltages and use a voltage-biased scanning tip to induce a movable local perturbation. We find that the scanning gate images differentiate reliably between the different regimes of electron transport. Our data are in good agreement with recent theories for interacting electron liquids in the ballistic and viscous regimes stimulated by measurements in graphene. However, the range of temperatures and densities where viscous effects are observable in Ga[Al]As are very distinct from the graphene material system.

DOI: 10.1103/PhysRevB.98.241304

Interparticle collisions dominate the behavior of fluids as described by hydrodynamic theory [1]. In degenerate, clean two-dimensional electron gases (2DEGs), e.g., realized in Ga[Al]As heterostructures or in graphene, hydrodynamic behavior may be expected if electron-electron interaction is the dominant scattering mechanism. At millikelvin temperatures, however, electron-impurity scattering dominates over electron-electron scattering. The latter produces only small corrections accounted for within Fermi-liquid theory, a description involving weakly interacting quasiparticles. The relevance of electron-electron scattering is enhanced by increasing the temperature, thus softening the Fermi surface. The electron-electron scattering length l_{ee} then reaches well below both the geometric device sizes and the momentum relaxation length. Early experiments realized this regime aiming at the identification of hydrodynamic effects in Ga[Al]As 2DEGs [2,3]. Very recently, experimental signatures of viscosity due to electron-electron interaction have been found in graphene [4,5], Ga[Al]As [6], $PdCoO_2$ [7], and WP_2 [8], and related theories have been developed [9–13].

Viscous flow gives rise to intricate spatial flow patterns occurring at length scales well below the Drude scattering length l_D, beyond which the momentum of the electronic system is dispersed [9–11]. Such spatial patterns in electronic systems have been theoretically predicted, but so far have not been imaged experimentally. This motivates us to perform scanning gate microscopy [14–16] measurements on a 2DEG in a Ga[Al]As heterostructure with signatures of viscous charge carrier flow. We find that the scanning gate measurement distinguishes the ballistic and viscous regimes of transport with high sensitivity. In the viscous regime, the scanning tip can locally revive ballistic contributions to the measured signals by introducing new and tunable length scales to the system geometry. Both a hydrodynamic and a ballistic model of electron transport guide us in interpreting the experimental data.

Following the experiments by Bandurin *et al.* [4,12] on graphene, we use vicinity voltage probes close to a local current injector to measure effects of viscosity. The concept of the measurement is sketched in Fig. 1(a). We pass a current I from the source contact through a 300-nm-wide orifice into a 5-μm-wide channel, which is connected to the drain contact at ground potential. The upper channel boundary has three additional openings to probe the vicinity voltages V_j at a distance d_j from the current-injecting orifice with d_j being 600, 1200, and 2400 nm, respectively. The vicinity voltages V_j are measured with respect to the reference potential V_{ref} at the right end of the channel. In this geometry one expects positive vicinity voltages for diffusive and ballistic electron motion in the channel, and negative values if electron-electron interaction is dominant [4,9,13]. In the latter case back-flow currents are proposed [11] as indicated by the schematic flow pattern in Fig. 1(a).

We use a Ga[Al]As heterostructure with a 2DEG buried 130 nm below the surface and a back-gate to tune the electron density n [17]. To measure the vicinity voltages we use low-noise voltage amplifiers and standard lock-in techniques at 31.4 Hz. We cool the sample in a cryostat equipped with an atomic force microscope to create a local perturbation by scanning gate microscopy (SGM).

We define the vicinity resistance as the ratio $R_j = V_j/I$ of the measured quantities, without offset subtraction. Figure 1(b) shows the vicinity resistances normalized to the 2DEG sheet resistance ρ as a function of temperature T from 30 mK to 30 K [18]. At the lowest temperature, all vicinity

*bbraem@phys.ethz.ch

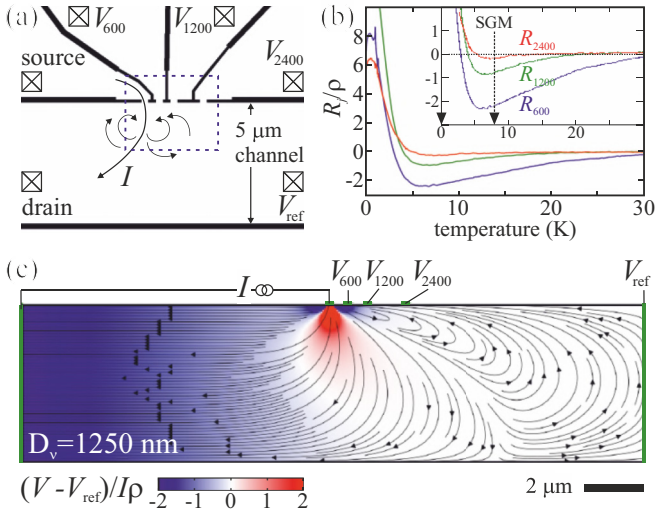

FIG. 1. (a) Top gates (indicated by black lines) deplete the 2DEG to shape the sample to a channel with orifices to the top region, which serve as current injector and voltage probes. The vicinity voltages V_j are measured with respect to the channel potential V_{ref}. Arrows indicate schematically the current distribution if back-flow occurs due to viscosity. The dashed rectangle marks the area where the tip of the scanning gate microscope is scanned. (b) Normalized vicinity resistances $R_j/\rho := (V_j - V_{\mathrm{ref}})/I\rho$ as a function of temperature in the absence of the SGM tip at $n = 1.2 \times 10^{11}\,\mathrm{cm}^{-2}$. The inset shows the same data enlarged to highlight the minima at around 7 K. The vertical dashed lines mark the temperatures of the SGM measurements in Fig. 2. (c) Current distribution and potential from solving the hydrodynamic model with a length scale parameter $D_\nu = 1.25\ \mu$m, which corresponds to $n = 1.2 \times 10^{11}\ \mathrm{cm}^{-2}$ and $T \approx 7$ K. The green lines mark equipotential surfaces forming the contacts to the channel.

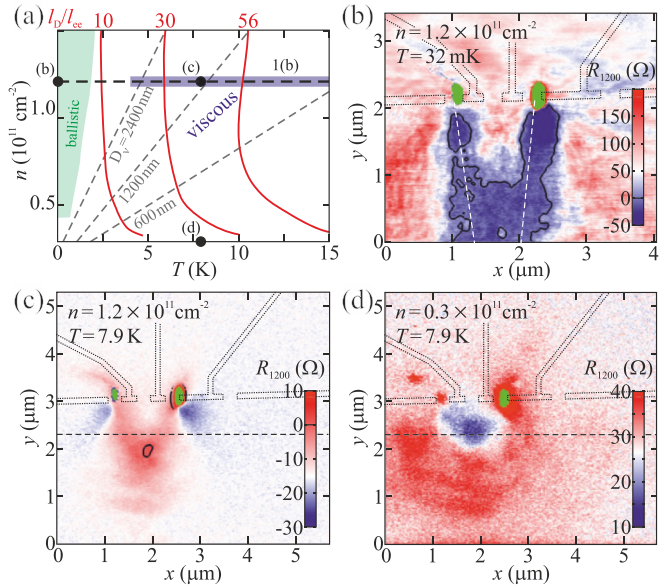

FIG. 2. (a) Schematic of transport regimes as a function of temperature and electron density. Viscous effects are expected at a high ratio $l_{\mathrm{D}}/l_{\mathrm{ee}}$. Red lines mark contours of $l_{\mathrm{D}}/l_{\mathrm{ee}}$ and show the increase with T and n. The green shade marks the ballistic regime where both l_{D} and l_{ee} exceed the channel width. Dashed gray lines indicate $D_\nu = d_j$. Three black dots mark the parameters of the SGM measurements in panels (b)–(d). The data shown in Fig. 1(b) is measured along the dashed black line; the blue shade indicates the temperature range of negative R_{1200}. (b)–(d) Vicinity resistance R_{1200} as a function of SGM tip position x, y with white color marking the value in the absence of the tip: (b) At 32 mK we observe a V shape of reduced $R_{1200}(x, y)$ along the white dashed lines, which mark the ballistic trajectory. Dotted lines mark the outlines of the gates, and areas of green color indicate tip positions leading to $I = 0$ or disconnected voltage probe. (c) At 7.9 K the vicinity resistance $R_{1200}(x, y)$ shows a maximum instead of the V. (d) $R_{1200}(x, y)$ at 7.9 K at lower electron density.

resistances are positive. With increasing T their signs change at around 3 K. The temperature of the zero-crossing increases with d_j. Furthermore, the vicinity resistances have a minimum at around 7 K and tend toward zero with increasing T. This behavior is similar to recent experiments in bilayer graphene [4,12].

To understand the behavior of the vicinity resistances as a function of temperature, in Fig. 1(b) we consider the scattering lengths l_{ee} and l_{D} of the 2DEG realized within the range of our experimental parameters. Figure 2(a) displays red contour lines of the ratio $l_{\mathrm{D}}/l_{\mathrm{ee}}$, where $l_{\mathrm{ee}} = v_{\mathrm{F}}\tau_{\mathrm{ee}}$ was calculated from τ_{ee} [19,20] and the Drude scattering length l_{D} was extracted from bulk resistance measurements [18]. One can see that $l_{\mathrm{D}}/l_{\mathrm{ee}} \gg 1$ in an extended region of the parameter space indicating where electron-electron interactions dominate. The horizontal dashed line marks the density of the measurement shown in Fig. 1(b). Two complementary theories exist describing the behavior along this line. Their applicability depends on the ratio l_{ee}/d_j.

The regime $l_{\mathrm{ee}} < d_j$ realized for $T \gtrsim 6$ K is described by the viscous theory [4,9,10]. Numerical calculations as in Ref. [4] based on the solution of the Navier-Stokes equation result in the flow patterns shown in Fig. 1(c) for our sample geometry. The intrinsic length scale of the theory $D_\nu = \sqrt{l_{\mathrm{ee}} l_{\mathrm{D}}/4}$ was chosen to match the experimental conditions at about 7 K. The theory predicts negative vicinity resistances of $R_{600}/\rho = -0.65$, $R_{1200}/\rho = -0.11$, and $R_{2400}/\rho = -0.015$, which are in qualitative agreement with the measurements in Fig. 1(b). With increasing temperature or d_j, D_ν falls below d_j and the vicinity voltage probes become insensitive to the quasilocal viscous effects. This is in accordance with R_j/ρ in Fig. 1(b) tending toward zero for high T.

For $l_{\mathrm{ee}} > d_j$, i.e., $T \lesssim 4$ K, diffusive transport between the injector and the voltage probe is not effective yet, and single electron-electron scattering events will dominate the measured vicinity voltages. This regime is described by the theory of Shytov *et al.* [13]. They propose that the vicinity voltage response is negative with its strength increasing with the electron-electron scattering rate, i.e., with temperature. This is in qualitative agreement with the strongly decreasing R_j around 3 K in Fig. 1(b).

At temperatures below 1.7 K, l_{ee} exceeds the width of the channel of our sample and both of the above-mentioned theories become inapplicable. An extended theory covering the full range of temperatures [12] proposes that the positive vicinity voltage observed in the experiment is caused by ballistic electron motion between the injector orifice and the

voltage probe with intermittent reflection at the opposite channel boundary. This claim is supported by the SGM measurements presented below.

We now scan the SGM tip at a fixed height of 40 nm, which allows for scanning over the top gates, above the GaAs surface in the area indicated by the dashed rectangle in Fig. 1(a). Applying a negative voltage to the tip creates a disk of depleted 2DEG with a diameter of approximately 300 nm. Within a distance of 1 μm around the tip position, the electron density smoothly approaches the bulk value [18]. We have taken scanning gate images for a range of back-gate voltages, contact configurations, and channel widths, but in the interest of brevity we present data for the three selected, most significant regimes marked by the black dots in Fig. 2(a).

Figure 2(b) shows the vicinity resistance R_{1200} as a function of the tip position x, y at $T = 32$ mK, in the ballistic regime where $l_D \approx 36\ \mu$m and $l_{ee} \gg l_D$. White color presents R_{1200} as measured in the absence of the tip. Blue indicates a reduced, and red an increased value of R_{1200}. The black contour at zero highlights the tip positions of sign inversion. For orientation, black dotted lines mark the outlines of the top gates. If the tip depletes the 2DEG in the source orifice or in the voltage probe opening, R_{1200} cannot be extracted and the position is colored green. The classical ballistic electron trajectory from the source to the voltage probe, that is once reflected by the channel gate, is indicated by white dashed lines. We observe a V-shaped reduction of R_{1200} along the outline of this ballistic path. We interpret the result in the following way: In the absence of the tip, some electrons are ballistically reflected by the channel gate into the voltage probe and we measure positive R_{1200}. For tip positions along the V-shaped ballistic path, the tip potential deflects ballistic trajectories and we observe a reduction of $R_{1200}(x, y)$. Conversely, a tip positioned outside the V guides additional trajectories into the voltage probe and thus increases $R_{1200}(x, y)$. Such a deflection of ballistic trajectories has been demonstrated by earlier SGM work [21–23].

We change to the viscous regime by heating the cryostat temperature to 7.9 K such that $l_D \approx 16\ \mu$m and $l_{ee} \approx 0.4\ \mu\text{m} < d_j$, leading to a characteristic length scale $D_\nu = 1.2\ \mu$m. Figure 2(c) shows the corresponding SGM measurement. The striking difference to Fig. 2(b) witnesses the change of the transport regime from ballistic to viscous. The V-shaped reduction of R_{1200} is no longer present. Consistent with the measurements in Fig. 1(b), $R_{1200}(x, y)$ is negative if the tip is far from the source orifice or the voltage probe, for example at $x > 5\ \mu$m. In contrast to measurements at lower temperature, $R_{1200}(x, y)$ features a maximum at $x \approx y \approx 2\ \mu$m. This distinguished position is approximately separated by d_{1200} from both the source orifice and the voltage probe. Here the tip forms a scattering site much closer than the lower channel edge at $y \approx -2\ \mu$m.

We now reduce the electron density to $n = 0.3 \times 10^{11}$ cm^{-2} while keeping the temperature at 7.9 K [see the point labeled (d) in Fig. 2(a)]. At this low density, $l_D \approx 1.6\ \mu$m and $l_{ee} \approx 70\ \text{nm} \ll d_j$, and the characteristic scale $D_\nu = 170$ nm has fallen well below d_j. Therefore we do not observe the effects of viscosity but a positive vicinity resistance in the absence of the tip. SGM at this low density finds $R_{1200}(x, y)$ presented in Fig. 2(d), which is significantly different to the result both in (b) and in (c) at four times higher electron density. Instead of a maximum we find a $R_{1200}(x, y)$ minimum at $x \approx 2\ \mu$m, $y \approx 2.3\ \mu$m.

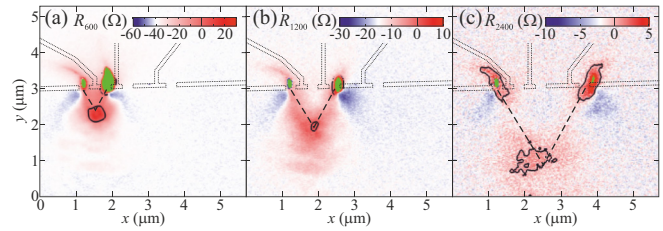

FIG. 3. All three vicinity resistances at $T = 7.9$ K and $n = 1.2 \times 10^{11}$ cm^{-2} as a function of tip position: (a) R_{600} and (b) R_{1200} as already shown in Figs. 2(c) and 2(d) R_{2400}. As indicated by the dashed lines, we find a maximum of R_j when the tip forms an equilateral triangle with the source orifice and the voltage probe.

In Fig. 3 we return to the high-density regime and compare all three vicinity resistances R_j measured at 7.9 K. Note that Fig. 3(b) reproduces Fig. 2(c) for convenience. The dashed lines form an equilateral triangle between the current-injecting orifice and the respective vicinity voltage probe. The tip of the triangle coincides with the maximum of R_j in all three images, suggesting a purely geometrical interpretation. It seems that the presence of the tip-induced potential in this symmetry point prevents the observation of viscous effects and reestablishes a positive vicinity voltage.

In conjunction with Figs. 1(b) and 2(a) we have already discussed the microscopic transport regimes which we now found to result in dramatic differences in the scanning gate images in Figs. 2(b)–2(d). In the remaining parts of the Rapid Communication, we discuss the imaging mechanism of the scanning gate technique in the viscous regime represented by Figs. 2(c) and 2(d). Naively one could think that the

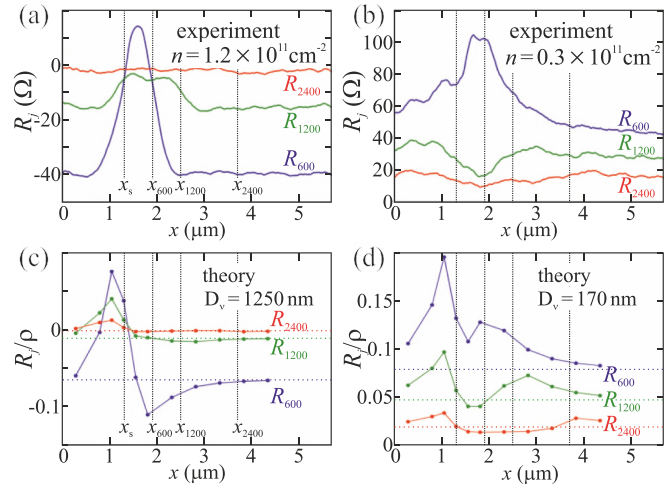

FIG. 4. Comparison between experiment and hydrodynamical model: (a),(b) R_j along the dashed lines in Figs. 2(c) and 2(d); the x coordinates x_j of source orifice and voltage probes are marked by the vertical lines. (c),(d) Vicinity resistances calculated with the hydrodynamic model for the tip positions and length scales D_ν in the experimental data of (a) and (b). The horizontal dotted lines denote the vicinity resistances in the absence of the tip.

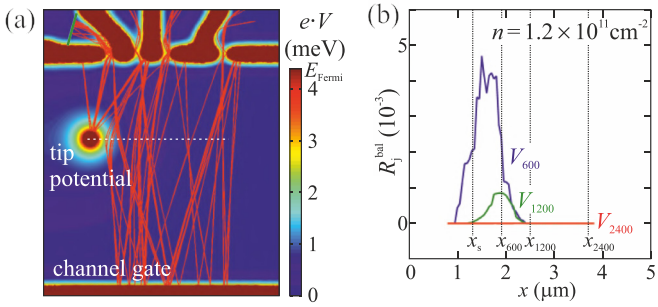

FIG. 5. Classical trajectories: (a) Color plot showing the potential landscape in the 2DEG from tip and top gates from finite element simulation. Red lines show classical trajectories starting at the green line in the source lead and ending in one of the voltage probes. (b) The number of trajectories ending in the voltage probes weighted by the trajectory length.

scanning tip-induced potential introduces a new internal sample boundary, which leads to a reorganization of the viscous flow pattern and thereby to a change in the vicinity voltages. We will therefore discuss the agreement and differences between the hydrodynamic model in Fig. 1(c) and the scanning gate measurements first.

The hydrodynamic model solves for the stationary flow of the classical incompressible viscous electron liquid at very low Reynolds numbers, where the nonlinear convective acceleration term in the Navier-Stokes equation can be neglected. Thanks to the addition of a Drude-like momentum relaxation rate, the resulting equations are well suited to describe the transition from the viscous to the momentum-scattering dominated regime [9]. However, this model does not account for ballistic effects. We solve the model in the presence of a local Lorentzian-shaped decrease of the electron density caused by the tip potential [18,24].

In Fig. 4 we compare the measured vicinity resistances along the dashed lines in Figs. 2(c) and 2(d) with the prediction of the model for the same tip positions and length scales D_ν. For orientation, the vertical lines mark the x coordinates of the source orifice and the voltage probes. In the high-density case in (a),(c) we find qualitative agreement for tip positions $x > 4\ \mu$m, but not at $x < 3\ \mu$m where the distance between the tip and the orifices is of the order of D_ν and no longer $\gg l_{ee}$. We speculate that the disagreement originates from the close, tip-induced scattering site which revives ballistic effects.

In the low-density case (b),(d) we find a rough agreement for all tip positions for R_{1200} and R_{2400}, but not for the signal R_{600} if the tip is close to the respective voltage probe. As in the high-density case, we find a disagreement if the distance between the tip and the orifices is of the order of D_ν. Since the hydrodynamic model does not describe ballistic effects, we consider this as a justification for the hypothesis, that the presence of the tip leads to a revival of ballistic effects in the sample on the small length scale introduced by the tip.

To test this hypothesis, we investigate ballistic contributions in a deliberately oversimplified classical model. We calculate electron trajectories emanating from the source orifice in the electrostatic potential of gates and tip exemplarily shown in Fig. 5(a). For tip positions along the dashed line we count the number of trajectories that end in one of the voltage probes as a qualitative measure for the ballistic contribution R_j^{bal} to the corresponding vicinity resistance. We count each trajectory with a weight that decreases exponentially with trajectory length to account for electron-electron scattering [18]. Figure 5(b) shows the resulting maxima of R_j^{bal} for the tip positions in the middle between the source orifice and the corresponding voltage probe. This is in agreement with the experimental observations at high density in Fig. 4(a), when the tip is close to the orifices. It supports our speculative interpretation that the resistance maxima in Fig. 3 result from an enhancement of ballistic contributions to the conductance, which quench the visibility of the viscous effects.

In summary, we have presented measurements of negative vicinity resistances in Ga[Al]As heterostructures, which indicate viscous behavior. By increasing the temperature we observed the transition from the ballistic to the viscous regime when the electron-electron scattering length falls below the separation between current injector and voltage probes. These findings are qualitatively similar to observations on graphene samples, but both the charge carrier density and the characteristic temperature are an order of magnitude lower. The movable perturbation by SGM introduces an additional, competing length scale. Scanning gate images in the ballistic and viscous regimes are markedly different. By forming a scattering site close to the source orifice and the voltage probes, ballistic effects can be restored even though the electron-electron scattering length is below the channel width. A hydrodynamic model explains some of the observed features including the negative vicinity resistances. From the difference between this model and the experiment we find that residual ballistic effects need to be considered on small length scales even at a high temperature of 7.9 K. The theory developed in Ref. [12] based on the kinetic equation is well suited to describe the transition between the ballistic and the viscous regime of transport. It therefore remains an interesting open question, if this approach could be used for describing the scanning gate experiment, and if it yields agreement with the experiment over a larger range of parameters. Furthermore, a less invasive measurement as proposed recently [25] could provide complementary information about the current distribution in the absence of the tip perturbation.

We thank Leonid Levitov and Yigal Meir for valuable discussions. The authors acknowledge financial support from ETH Zürich and from the Swiss National Science Foundation (NCCRQSIT, SNF 2-77255-14).

[1] L. D. Landau and E. M. Lifshitz, *Fluid Mechanics*, 2nd ed. (Butterworth-Heinemann, Amsterdam, 1987), Vol. 6.

[2] L. W. Molenkamp and M. J. M. de Jong, Solid-State Electron. **37**, 551 (1994).

[3] M. J. M. de Jong and L. W. Molenkamp, Phys. Rev. B **51**, 13389 (1995).
[4] D. A. Bandurin, I. Torre, R. K. Kumar, M. B. Shalom, A. Tomadin, A. Principi, G. H. Auton, E. Khestanova, K. S. Novoselov, I. V. Grigorieva, L. A. Ponomarenko, A. K. Geim, and M. Polini, Science **351**, 1055 (2016).
[5] J. Crossno, J. K. Shi, K. Wang, X. Liu, A. Harzheim, A. Lucas, S. Sachdev, P. Kim, T. Taniguchi, K. Watanabe, T. A. Ohki, and K. C. Fong, Science **351**, 1058 (2016).
[6] G. M. Gusev, A. D. Levin, E. V. Levinson, and A. K. Bakarov, AIP Adv. **8**, 025318 (2018).
[7] P. J. W. Moll, P. Kushwaha, N. Nandi, B. Schmidt, and A. P. Mackenzie, Science **351**, 1061 (2016).
[8] J. Gooth, F. Menges, N. Kumar, V. Süß, C. Shekhar, Y. Sun, U. Drechsler, R. Zierold, C. Felser, and B. Gotsmann, Nat. Commun. **9**, 4093 (2018).
[9] I. Torre, A. Tomadin, A. K. Geim, and M. Polini, Phys. Rev. B **92**, 165433 (2015).
[10] L. Levitov and G. Falkovich, Nat. Phys. **12**, 672 (2016).
[11] F. M. D. Pellegrino, I. Torre, A. K. Geim, and M. Polini, Phys. Rev. B **94**, 155414 (2016).
[12] D. A. Bandurin, A. V. Shytov, L. S. Levitov, R. K. Kumar, A. I. Berdyugin, M. B. Shalom, I. V. Grigorieva, A. K. Geim, and G. Falkovich, Nat. Commun. **9**, 4533 (2018).
[13] A. Shytov, J. F. Kong, G. Falkovich, and L. Levitov, Phys. Rev. Lett. **121**, 176805 (2018).
[14] M. A. Eriksson, R. G. Beck, M. Topinka, J. A. Katine, R. M. Westervelt, K. L. Campman, and A. C. Gossard, Appl. Phys. Lett. **69**, 671 (1996).
[15] M. A. Topinka, B. J. LeRoy, S. E. J. Shaw, E. J. Heller, R. M. Westervelt, K. D. Maranowski, and A. C. Gossard, Science **289**, 2323 (2000).
[16] M. A. Topinka, B. J. LeRoy, R. M. Westervelt, S. E. J. Shaw, R. Fleischmann, E. J. Heller, K. D. Maranowski, and A. C. Gossard, Nature (London) **410**, 183 (2001).
[17] M. Berl, L. Tiemann, W. Dietsche, H. Karl, and W. Wegscheider, Appl. Phys. Lett. **108**, 132102 (2016).
[18] See Supplemental Material at http://link.aps.org/supplemental/10.1103/PhysRevB.98.241304 for experimental details, 2DEG properties, electron-scattering lengths, and a detailed description of the models.
[19] T. Jungwirth and A. H. MacDonald, Phys. Rev. B **53**, 7403 (1996).
[20] G. Giuliani and G. Vignale, *Quantum Theory of the Electron Liquid*, 1st ed. (Cambridge University Press, Cambridge, 2008).
[21] R. Crook, C. G. Smith, M. Y. Simmons, and D. A. Ritchie, Phys. Rev. B **62**, 5174 (2000).
[22] K. E. Aidala, R. E. Parrott, T. Kramer, E. J. Heller, R. M. Westervelt, M. P. Hanson, and A. C. Gossard, Nat. Phys. **3**, 464 (2007).
[23] S. Bhandari, G.-H. Lee, A. Klales, K. Watanabe, T. Taniguchi, E. Heller, P. Kim, and R. M. Westervelt, Nano Lett. **16**, 1690 (2016).
[24] M. A. Eriksson, R. G. Beck, M. A. Topinka, J. A. Katine, R. M. Westervelt, K. L. Campman, and A. C. Gossard, Superlattices Microstruct. **20**, 435 (1996).
[25] K. A. Guerrero-Becerra, F. M. D. Pellegrino, and M. Polini, arXiv:1810.07573.